

1
2
3
4
5
6
7
8
9
10
11
12
13
14
15
16
17
18
19
20
21
22
23
24
25

UNIVERSITY OF CALIFORNIA
SANTA CRUZ

**AN INCLUSIVE SEARCH FOR THE DECAY OF A BOOSTED
HIGGS BOSON IN THE $H \rightarrow b\bar{b}$ CHANNEL WITH THE ATLAS
DETECTOR**

A dissertation submitted in partial satisfaction of the
requirements for the degree of
DOCTOR OF PHILOSOPHY

in

PARTICLE PHYSICS

by

Jacob Martin Pasner

October 2019

The Dissertation of Jacob Martin Pasner
is approved:

Professor Jason Nielsen, Chair

Professor Abraham Seiden

Professor Michael Hance

Dean Lori Kletzer
Vice Provost and Dean of Graduate Studies

Copyright © by

Jacob Martin Pasner

2019

31 **Table of Contents**

32	List of Figures	vii
33	List of Tables	ix
34	Abstract	x
35	Dedication	xi
36	Acknowledgments	xii
37	1 Introduction	1
38	I Theoretical Motivations and the Standard Model	2
39	2 The Standard Model and Beyond	3
40	2.1 The Standard Model	4
41	2.1.1 Bosons	5
42	2.1.2 Fermions	8
43	2.2 Quantum Electrodynamics	8
44	2.3 Quantum Chromodynamics	12
45	2.4 Spontaneous Symmetry Breaking	14

46	2.5	The Higgs Mechanism	14
47	II	Experimental Apparatus and Associated Facilities	15
48	3	The Large Hadron Collider	16
49	3.1	Particle Incjecton Chain	17
50	3.2	LHC layout and design	19
51	3.3	Performance	22
52	3.4	Pile-up at the LHC	24
53	4	The ATLAS Detector	26
54	4.1	ATLAS Coordinate System	29
55	4.2	Tracking with the Inner Detector	33
56	4.2.1	Pixel Detector	35
57	4.2.2	Semiconductor Tracker	35
58	4.2.3	Transition Radiation Tracker	36
59	4.3	Calorimetry	37
60	4.3.1	Electromagnetic Calorimeter	38
61	4.3.2	Hadronic Calorimeter	40
62	4.4	Muon Spectrometer	42
63	5	Boosted Higgs at the LHC	45
64	5.1	Physics beyond the Stnadard Model	46
65	5.2	Higgs Production Mechanisms	46
66	5.3	Branching Ratios	46
67	5.4	Discovery	46
68	5.5	Fermion Decay Modes	46

69	5.6 Boosted Higgs	46
70	III The HbbISR Analysis	47
71	6 Data and Simulation Preparation	48
72	6.1 Data Used	48
73	6.2 Monte Carlo Samples	48
74	7 Physics Object Selection	49
75	7.1 Calorimeter Jets	50
76	7.2 Track Jets	50
77	7.3 Fat Jets	50
78	7.4 B-tagged Jets	50
79	7.5 Muons	50
80	7.6 Overlap Removal	50
81	8 Event Selection	51
82	8.1 Selected Triggers	51
83	8.2 Pre-selection Studies	51
84	8.3 Signal Selection	51
85	8.4 Optimisation	51
86	9 Background Estimation	52
87	9.1 Multi-jet QCD estimation	52
88	9.2 $t\bar{t}$ control region	52
89	9.3 Single top estimation	52
90	9.4 Hadronic vector boson channel	52

91	10 Systematic Uncertainties	53
92	10.1 Theoretical Uncertainties	53
93	10.2 Experimental Uncertainties	53
94	11 Statistical Fit	54
95	11.1 Profile Likelihood Function	54
96	11.2 Fit Configuration	54
97	11.3 Statistical Tests	54
98	12 Results	55
99	12.1 Expectations	55
100	12.2 Statistical Analysis Results	55
101	12.3 Measurements and Limits	55
102	IV Conclusion	56
103	13 Conclusion	57
104	Bibliography	57
105	A Hadronic Vqq Sherpa Studies	60

106 List of Figures

107	2.1	Summary of several Standard Model total and fiducial production cross	
108		section measurements, corrected for leptonic branching fractions, com-	
109		pared to the corresponding theoretical expectations. All theoretical ex-	
110		pectations were calculated at NLO or higher. The dark-color error bar	
111		represents the statistical uncertainty. The lighter-color error bar repre-	
112		sents the full uncertainty, including systematics and luminosity uncer-	
113		tainties. The data/theory ratio, luminosity used and reference for each	
114		measurement are also shown. Uncertainties for the theoretical predictions	
115		are quoted from the original ATLAS papers. They were not always eval-	
116		uated using the same prescriptions for PDFs and scales. The Wgamma	
117		and Zgamma theoretical cross-sections have non-perturbative corrections	
118		applied to the NNLO fixed order calculations (PRD 87, 112003 (2013)).	
119		Not all measurements are statistically significant yet.	6
120	2.2	Table of all observed fundamental particles of the current Standard Model.	7
121	3.1	CERN accelerator complex	18
122	3.2	Labeled diagram of all the experiments at the LHC indicating the counter	
123		circulating beams and points of interest along the circumference of the	
124		accelerator.	20
125	3.3	Depiction of a LHC dipole magnet 2-in-1 design labeling the major com-	
126		ponents	21
127	3.4	Luminosity is monitored as both a running total known as the Integrated	
128		Luminosity as depicted in (a) and as an instantaneous quantity as shown	
129		in (b)	24
130	3.5	Pileup for data taking periods 2015 - 2018	25

131	4.1	[3] Here we see a cut-away side view of the ATLAS detector with the	
132		major components labeled. Note that within each of these labeled com-	
133		ponents there may exist multiple different detector technologies. For scale	
134		two people in red are shown standing between the disk muon chambers	
135		on the left side of the figure.	27
136	4.2	This slice of the ATLAS detector depicts how different particles interact	
137		with each component of the detector it crosses. A dashed line indicates	
138		no interaction while a solid line indicates interaction. Electrons (yel-	
139		low/green) and charged hadrons (red) interact with the tracker and curve	
140		in the solenoid's magnetic field. Electrons and photons (yellow/green) are	
141		absorbed by the Electromagnetic calorimeter. All hadrons (red/yellow)	
142		are absorbed by the Hadronic calorimeter. The muons (orange) curve in	
143		both the solenoid and torroid magnetic fields before exiting the detector.	
144		Finally, the neutrinos (white) pass through the entire detector without	
145		interacting.	30
146	4.3	[4] A cartoon view of the the LHC from above showing the SPS, LHC	
147		and the four main experiments of the LHC: ATLAS, CMS, LHCb, and	
148		ALICE. The standard cartesian coordinate system is shown with its origin	
149		at the ATLAS interaction point, the positive x -axis towards the center	
150		of the LHC, the positive y -axis pointing upwards, and the positive z -axis	
151		pointing along the beamline towards the "A-side"	31
152	4.4	Modified from [4] this cartoon represents a selection of pseudorapidity	
153		(η) values overlaid with some cartesian coordinates (dashed black lines).	
154		The redlines are drawn for $\eta = \pm 0.5, 1.0, 3.0$	32
155	4.5	[5] Diagram of inner detector	33
156	4.6	[8] Schematic of the Inner Detector including eta lines. Each component	
157		shown is cylindrically symmetric leading to a multi-layered detector. . .	34
158	4.7	[3] A cutaway diagram of ATLAS's sampling calorimeters	37
159	4.8	[3] Sketch of LAr EMC barrel module where the lead and liquid argon	
160		layers are visible in an accordion like geometry. Looking from the fore-	
161		ground to the back there are 3 different types of cells visible.	39
162	4.9	[3] Schematic of a tile calorimeter module including a depiction of the con-	
163		nection between the scintillator tile to the photomultiplier via a wavelength-	
164		shifting fibre.	41
165	4.10	[3] A cut-away diagram of the ATLAS muon system and its many sub-	
166		detectors.	43

¹⁶⁷ **List of Tables**

Abstract

An Inclusive Search for the decay of a Boosted Higgs boson in the $H \rightarrow b\bar{b}$

channel with the ATLAS detector

by

Jacob Martin Pasner

Abstract placeholder

174

Dedication

175

Dedication

176

Dedication

Acknowledgments

178 Chapter 1

179 Introduction

180 Every dissertation should have an introduction. You might not realize it, but the
181 introduction should introduce the concepts, backgrouand, and goals of the dissertation.

182

Part I

183

Theoretical Motivations and the

184

Standard Model

Chapter 2

The Standard Model and Beyond

The Standard Model (SM) of Particle Physics is humanities best "guess" at the force laws that describe the observed behavior of all particles in our universe. Its formulation is a collection of Quantum Field Theories (QFT) that describe the following interactions of elementary matter in Nature: the electromagnetic force, the weak nuclear force and the strong nuclear force. Gravity is noticeably absent as currently there is no viable quantum theory for observed gravitational effects. The Glashow-Salam-Weinberg (GSW) theory of Quantum Electrodynamics (QED) describes the electromagnetic and weak forces, while Quantum Chromodynamics (QCD) describes the strong force. These theories form the following symmetry group of the Standard Model.

$$\underbrace{\mathrm{SU}_C(3)}_{\mathrm{QCD}} \otimes \underbrace{\mathrm{SU}_L(2) \otimes \mathrm{U}_Y(1)}_{\mathrm{GSW}}. \quad (2.1)$$

196 The gauge principle states that the SM Lagrangian and its predictions must be invariant
197 under local transformations using an operator from any of these constituent groups.
198 Thus, any theory must only include transformations and terms that maintain the local
199 invariance of the complete Lagrangian. In particular, this requirement was violated
200 by any attempt to include an explicit mass term for the Gauge Bosons of QED and
201 for all fermions. Around 1960 a possible solution to this lack of mass was proposed
202 in the form of the spontaneous breaking of the ElectroWeak symmetry, now known as
203 the Higgs mechanism. In the following sections I will go into more detail about the
204 Lagrangian formalism of the Standard Model, QCD, QED and this recently verified
205 Higgs Mechanism.

206 **2.1 The Standard Model**

207 At the turn of the 20th century our understanding of the constituent matter of the uni-
208 verse was limited to what we could see with microscopes and imply from the observations
209 of light and electricity, giving us evidence for both the photon and the electron. In the
210 first half of the century we discovered the field of subatomic physics with Rutherford's
211 1911 gold foil scattering experiment, and Dirac successfully demonstrated the quantiza-
212 tion of the electromagnetic field, the first step towards a fully Gauge Invariant Quantum
213 Field Theory. In the second half we literally delved deeper, discovering that the nucleus
214 contained structure and extended our theories to include the the complex mechanics of
215 quarks and gluons. With the discovery of the Higgs in 2013 the Standard Model has

216 become an irrefutable framework as can be seen in the high level of agreement between
217 theory and experiment in figure 2.1.

218 The QCD and QED theories predict two classes of particles: fermions and bosons shown
219 in figure 2.2. These particles represent the quanta of the quantum fields of the Standard
220 Model and the mediators of the fundamental forces of Nature.

221 2.1.1 Bosons

222 These spin-1 particles are known as the vector gauge bosons and are the force carriers
223 of the SM. The most commonly known is the electromagnetic force's un-charged and
224 massless photon (γ) which interacts with all charged particles and is often referred to
225 as "light". The weak nuclear force is involved in nuclear interactions such as beta
226 decays and is carried by 3 bosons all of which have mass and couple to all fermions;
227 the W^\pm bosons, which mediate the charged weak nuclear interaction and allow for
228 flavor changing currents; and the Z boson which mediates the neutral weak nuclear
229 interaction. Finally we have 8 massless gluons which mediate the strong nuclear force
230 and only interact with fermions with a "color" charge such as the quarks contained
231 inside the nucleus. The only spin-0 boson, the Higgs Boson (h) is the key to generating
232 mass terms in the SM Lagrangian for the massive Gauge Bosons and for fermions. This
233 is done through the so called Higgs Mechanism and is discussed in more detail in section
234 2.5.

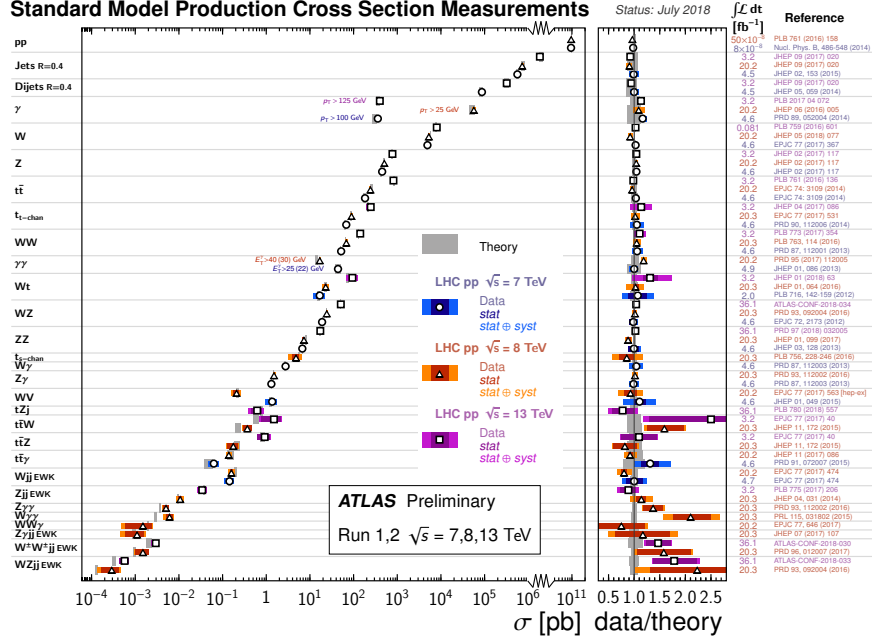


Figure 2.1: Summary of several Standard Model total and fiducial production cross section measurements, corrected for leptonic branching fractions, compared to the corresponding theoretical expectations. All theoretical expectations were calculated at NLO or higher. The dark-color error bar represents the statistical uncertainty. The lighter-color error bar represents the full uncertainty, including systematics and luminosity uncertainties. The data/theory ratio, luminosity used and reference for each measurement are also shown. Uncertainties for the theoretical predictions are quoted from the original ATLAS papers. They were not always evaluated using the same prescriptions for PDFs and scales. The $W\gamma$ and $Z\gamma$ theoretical cross-sections have non-perturbative corrections applied to the NNLO fixed order calculations (PRD 87, 112003 (2013)). Not all measurements are statistically significant yet.

Standard Model of Elementary Particles

three generations of matter (fermions)						interactions / force carriers (bosons)	
	I	II	III				
QUARKS	mass charge spin $\approx 2.2 \text{ MeV}/c^2$ $\frac{2}{3}$ $\frac{1}{2}$ u up	$\approx 1.28 \text{ GeV}/c^2$ $\frac{2}{3}$ $\frac{1}{2}$ c charm	$\approx 173.1 \text{ GeV}/c^2$ $\frac{2}{3}$ $\frac{1}{2}$ t top	$\approx 124.97 \text{ GeV}/c^2$ 0 0 1 g gluon			
	$\approx 4.7 \text{ MeV}/c^2$ $-\frac{1}{3}$ $\frac{1}{2}$ d down	$\approx 96 \text{ MeV}/c^2$ $-\frac{1}{3}$ $\frac{1}{2}$ s strange	$\approx 4.18 \text{ GeV}/c^2$ $-\frac{1}{3}$ $\frac{1}{2}$ b bottom	0 0 1 γ photon			
	$\approx 0.511 \text{ MeV}/c^2$ -1 $\frac{1}{2}$ e electron	$\approx 105.66 \text{ MeV}/c^2$ -1 $\frac{1}{2}$ μ muon	$\approx 1.7768 \text{ GeV}/c^2$ -1 $\frac{1}{2}$ τ tau	$\approx 91.19 \text{ GeV}/c^2$ 0 0 1 Z Z boson			
LEPTONS	$< 2.2 \text{ eV}/c^2$ 0 $\frac{1}{2}$ ν_e electron neutrino	$< 0.17 \text{ MeV}/c^2$ 0 $\frac{1}{2}$ ν_μ muon neutrino	$< 18.2 \text{ MeV}/c^2$ 0 $\frac{1}{2}$ ν_τ tau neutrino	$\approx 80.39 \text{ GeV}/c^2$ ± 1 1 W W boson			
					SCALAR BOSONS	GAUGE BOSONS VECTOR BOSONS	

Figure 2.2: Table of all observed fundamental particles of the current Standard Model.

235 2.1.2 Fermions

236 These spin-1/2 particles can be further broken up into two distinct families of particles,
237 the leptons and the quarks, both of which contain three "generations" each with an "up"
238 and "down" type particle. The leptons "up" type members are the electrically charged
239 electron (e), muon (μ) and tau (τ) while the "down" type are their electrically neutral
240 counterparts ν_e , ν_μ , ν_τ . The quarks "up" type members are the up (u), charm (c),
241 and top (t) each with a $+2/3$ elementary charge, while the "down" type members are
242 the down (d), strange (s), and bottom (b) all of which have a $-1/3$ elementary charge.
243 Each quark carries a "color" charge thus allowing them to participate in strong force
244 interactions. Due to the observed color confinement of the strong force these quarks are
245 only observed in colorless bound states known as "mesons" (1 quark and 1 anti-quark)
246 and "baryons" (an odd number of quarks and anti-quarks). All of the above fermions
247 have an anti-particle partner which has the opposite electrical charge but is otherwise
248 identical.

249 2.2 Quantum Electrodynamics

250 In the SM the Electromagnetic and Weak nuclear forces are unified into the Electroweak
251 interaction which is represented by the $SU(2)_L \times U(1)_Y$ gauge group. The L represents
252 the physical observable that the Weak interaction, and thus the $SU(2)$ transformation,
253 only acts on left handed particle states. The Y states that this is the $U(1)$ symmetry

254 for the weak hypercharge Y instead of the electromagnetic charge. The particle states
 255 for these interactions are solutions to the Dirac equation and are represented as Dirac
 256 spinor doublets (Ψ_L) for the left handed states, and as Dirac spinor singlets (Φ_R) for
 257 the right handed states. Thus when a general transformation from the Electroweak
 258 gauge group is applied to the left handed spinor doublet you get equation 2.2

$$\Psi_L \rightarrow \Psi'_L = \exp \left(\underbrace{ig' \frac{Y_L}{2} \zeta(x)}_{U(1)_Y} + \underbrace{ig_W \boldsymbol{\alpha}(x) \cdot \mathbf{T}}_{SU(2)_L} \right) \Psi_L. \quad (2.2)$$

259 For the right handed spinor singlet the $SU(2)_L$ doesn't contribute and you get equation
 260 2.3

$$\Phi_R \rightarrow \Phi'_R = \exp \left(\underbrace{ig' \frac{Y_R}{2} \zeta(x)}_{U(1)_Y} \right) \Phi_R. \quad (2.3)$$

261 We can see that these local gauge transformations have introduced space-time depen-
 262 dant terms $\boldsymbol{\alpha}(x)$ and $\zeta(x)$ into our electroweak Lagrangian. Due to the derivatives
 263 contained within the kinetic term of this lagrangian, this new configuration would in-
 264 troduce additional terms, thus violating our required local gauge invariance. Luckily,
 265 we can remove these additional terms by replacing the standard derivative (∂_μ) with th
 266 covariant derivative (D_μ) as seen in equation 2.4 for the left handed states and 2.5 for

267 the right handed states.

$$D_\mu = \partial_\mu - \underbrace{\frac{1}{2}ig' B_\mu Y_L}_{U(1)_Y} - \underbrace{\frac{1}{2}ig_W \mathbf{W}_\mu \cdot \boldsymbol{\tau}}_{SU(2)_L} \quad (2.4)$$

$$D_\mu = \partial_\mu - \underbrace{\frac{1}{2}ig' B_\mu Y_R}_{U(1)_Y} \quad (2.5)$$

268 Here we see two new gauge fields; B_μ the weak hypercharge field and \mathbf{W}_μ the charged
 269 weak field. The form of these fields is chosen such that the final Lagrangian is invariant
 270 under $SU(2)_L \times U(1)_Y$ transformations, and thus we have restored gauge invariance for
 271 the kinetic term of our electroweak Lagrangian! Inserting these new definitions into the
 272 Lagrangian for the spinor field Ψ which satisfies the free-particle Dirac equation we get

$$\mathcal{L} = i\bar{\Psi}_L \gamma^\mu \left(\partial_\mu - \frac{1}{2}ig' B_\mu Y_L - \frac{1}{2}ig_W \mathbf{W}_\mu \cdot \boldsymbol{\tau} \right) \Psi_L + i\bar{\Phi}_R \gamma^\mu \left(\partial_\mu - \frac{1}{2}ig' B_\mu Y_R \right) \Phi_R \quad (2.6)$$

273 Next we must construct the gauge field self interaction and mass terms

$$\mathcal{L} = -\frac{1}{4}\mathbf{F}_{\mu\nu}\mathbf{F}^{\mu\nu} - \frac{1}{4}B_{\mu\nu}B^{\mu\nu} + \frac{1}{2}M_W^2 \mathbf{W}_\mu \mathbf{W}^\mu + \frac{1}{2}M_B^2 B_\mu B^\mu \quad (2.7)$$

274 where the field tensors $\mathbf{F}^{\mu\nu}$ and $B^{\mu\nu}$ are defined to be

$$\mathbf{F}^{\mu\nu} = \partial^\mu \mathbf{W}^\nu - \partial^\nu \mathbf{W}^\mu + g \mathbf{W}^\mu \times \mathbf{W}^\nu \quad (2.8)$$

$$B^{\mu\nu} = \partial^\mu \mathbf{B}^\nu - \partial^\nu \mathbf{B}^\mu \quad (2.9)$$

275 The field tensor terms in equation 2.7 are invariant under our gauge transformations,
 276 but simply plugging in equation 2.4 or equation 2.5 into the mass terms shows that
 277 these terms violate gauge invariance thus implying $M_W = 0$ and $M_B = 0$ in direct
 278 contradiction of the observed masses of the weak gauge bosons. This issue arises again
 279 for fermion mass terms as illustrated below for the electron field (e) expanded in its chiral
 280 basis.

$$m\bar{e}e = m \begin{pmatrix} e_R^\dagger & e_L^\dagger \end{pmatrix} \begin{pmatrix} e_L \\ e_R \end{pmatrix} = m(e_R^\dagger e_L + e_L^\dagger e_R) \quad (2.10)$$

281 Remembering that the left and right handed spinors of the electroweak interaction trans-
 282 form differently we see that this mixture of right and left fields violates gauge invariance.
 283 This again forces us to conclude that $m = 0$ in contradiction to the observation that
 284 fermions do indeed have mass. As mentioned in section 2.1.1 the resolution to these
 285 mass mysteries lies in the Higgs mechanism discussed in section 2.5

2.3 Quantum Chromodynamics

Quantum Chromodynamics is the continuation of the mathematical framework established by Quantum Electrodynamics (section 2.2, this time for the strong force described by the $SU(3)_C$ gauge group where the C represents the "color" charge of QCD. This color charge doesn't imply actual visible color, but is useful as an analogy to the visible spectrum where a combination of red, green, and blue generates white. For QCD the combination of red, green, and blue color charges results in a colorless object. As mentioned in section 2.1.2 the quarks will contain a color (anti-color) charge represented by a color triplet field which transforms under the general $SU(3)$ transformation as shown here

$$q = \begin{pmatrix} q_r \\ q_g \\ q_b \end{pmatrix} \rightarrow q' = \exp \left(ig_s \sum_{k=1}^8 \eta_k(x) \frac{\lambda_k}{2} \right) q \quad (2.11)$$

Here the λ_k are the generators for $SU(3)$, $\eta(x)_k$ is the space-time dependency for each generator, and g_s is the strong coupling constant. As with QED, the introduction of these space-time dependant terms introduces new terms into the kinematic portion of the lagrangian thus spoiling our gauge invariance. Again, we introduce a covariant

300 derivative to restore invariance

$$D_\mu = \partial_\mu - ig_s G_\mu^k \frac{\lambda_k}{2} \quad (2.12)$$

301 Here the G_μ^k are the new fields introduced for the 8 gluons. These new fields transform
 302 under $SU(3)$ as shown in equation ??

$$G_\mu^k \rightarrow G_\mu'^k = G_\mu^k + \partial_\mu \eta_k(x) + g_s f_{klm} \eta_l(x) G_\mu^m \quad (2.13)$$

303 Given these definitions we can construct the QCD Lagrangian (\mathcal{L}_{QCD}) as shown in
 304 equation 2.14 where the gluon field tensor $G_k^{\mu\nu}$ is the one defined in equation 2.15

$$\mathcal{L}_{QCD} = \bar{q}(i\gamma_\mu D^\mu - m_q)q - \frac{1}{4} G_k^{\mu\nu} G_{k\mu\nu} \quad (2.14)$$

$$G_k^{\mu\nu} = \partial^\mu G_k^\nu - \partial^\nu G_k^\mu + g_s f_{klm} G_l^\mu G_m^\nu \quad (2.15)$$

305 The strong force is peculiar in that we experimentally observe only colorless objects in
 306 the form of bound states of quarks known as hadrons. Qualitatively, when a bound
 307 state of quarks (meson or baryon) is given sufficeint energy to separate the strong force
 308 dramatically increases in strength. At the point where the objects would separate, and
 309 thus no longer be colorless, it becomes energetically favorable to produce a quark/anti-
 310 quark pair. In other words, attempting to separate a bound quark state into its colored

311 constituents simply results in new colorless bound states. This requirement of colorless
312 objects by the strong force is known as color confinement.

313 **2.4 Spontaneous Symmetry Breaking**

314 Spontaneous symmetry breaking occurs when a system loses an inherent symmetry in
315 order to attain a lower energy configuration.

316 **2.5 The Higgs Mechanism**

317 The Higgs Mechanism is the system by which particles attain mass through the spon-
318 taneous breaking of the Higgs potential, thus causing all particles it interacts with to
319 have mass.

320

Part II

321

Experimental Apparatus and

322

Associated Facilities

323 Chapter 3

324 The Large Hadron Collider

325 Located 100 meters under the Swiss / French boarder lies the 26.7 kilometer Large
326 Hadron Collider (LHC) [1]. The culmination of a huge international collaboration,
327 this apparatus is used to produce proton and heavy ion collisions for observation by the
328 four major experiments at the LHC: ATLAS, CMS, LHCb, and ALICE. The system was
329 designed for a maximum center-of-mass energy of $\sqrt{s} = 14$ TeV and a peak instantaneous
330 luminosity of $L = 10^{34} \text{cm}^{-2} \text{s}^{-1}$.

331 The first LHC workshop was held in 1984 in Lausanne at the European Organization
332 for Nuclear Reserach (CERN) [2]. The nearly 30 year old case for a machine that
333 would push towards the discovery of the elusive Higgs Boson was presented using the
334 existing CERN accerlerator facilities and the Large Electron Positron (LEP) collider
335 tunnel. The proposal became reality on September 10, 2008 when the first proton beams
336 were circulated, only to have calamity strike 9 days later in the form of a catastrophic

337 electrical fault. The repairs and improvements lasted until November 2009 when the
338 LHC restarted. Since then this modern marvel has worked wonderfully and, as hoped,
339 lead to the discovery of the Higgs Boson by the CMS and ATLAS collaborations July
340 4, 2013.

341 The following chapter provides a brief introduction to the worlds most powerful accel-
342 erator starting with the little red bottle of hydrogen in building XXX, and ending with
343 the interaction point where protons collide at the highest energies ever produced.

344 **3.1 Particle Injecton Chain**

345 We begin with the most common element in the Universe, hydrogen, as our source of
346 protons. A bottle of hydrogen gas provides 100 microsecond pulses of raw H_2 which
347 is then injected into a Duoplasmatron. There, a strong electric field and free elctrons
348 from a cathode ionize the molecule into bare H^+ aka a proton! These protons are
349 then accelerated by a 90kV field, leaving the Duoplasmatron with 1.4% speed of light
350 ($\sim 4000\text{km/s}$) or, in relativistic units, about 83KeV. The bare protons are then fed
351 into the accelerating RadioFrequency (RF) cavities of Linear Accelerator 2 (LINAC2).
352 Inside, conductors charged by a powerful oscillating electromagnetic field accelerate the
353 protons resulting in a 50MeV energy. Along the way, small quadrupole magnets shape
354 the proton packet insuring they remain in a tight beam. This pattern of accleration
355 with RF cavities and shaping/turnig with magnets is then repeated with CERN's first

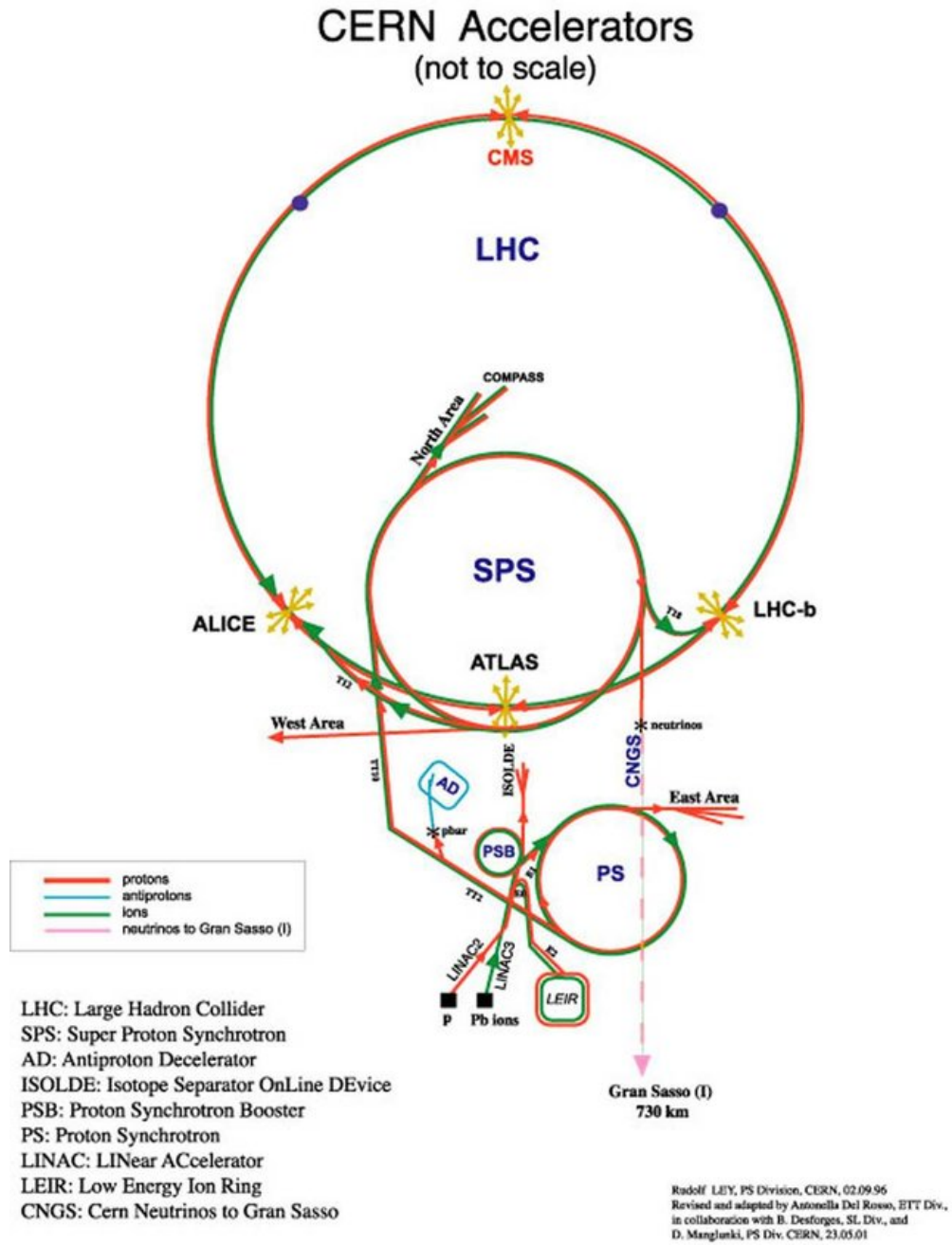


Figure 3.1: CERN accelerator complex

356 synchrotron, the Proton Synchrotron (PS) rendering a 1.4 GeV beam. The final step
357 before the LHC comes with the Super Proton Synchrotron where the same technologies
358 are implemented to produce 450 GeV protons, ready for injection into the LHC. A
359 diagrammatic representation of this chain can be seen in figure 3.1

360 In order to produce proton-proton collisions the LHC uses two beams circulating in
361 opposite directions. The beams are not continuous, but instead consist of bunches, or
362 buckets, of $\mathcal{O}(10^{11})$ protons with a spacing of 25ns. Given the LHC circumference this
363 allows for 3564 buckets, however only 2808 are filled per beam due to safety requirements
364 and injection limitations. Each beam takes 4 minutes and 20 seconds to fill and then an
365 additional 20 minutes to for the protons to reach their maximum energy of 7 TeV TeV,
366 or 99.99999991% the speed of light! Under normal operating conditions these beams
367 can be used for many hours.

368 **3.2 LHC layout and design**

369 While often depicted as a perfect circle the LHC is in reality an octagon with rounded
370 edges, called arcs, as can be seen in figure 3.2. Here you can see the counter circulating
371 beams of protons depicted in red and blue. These beams are focused and collided at
372 the 4 dedicated interaction points at rates of up to 40 MHz. Two of these points are
373 occupied by the ATLAS and CMS experiments, both of which are high luminosity,
374 multi-purposed experiments.

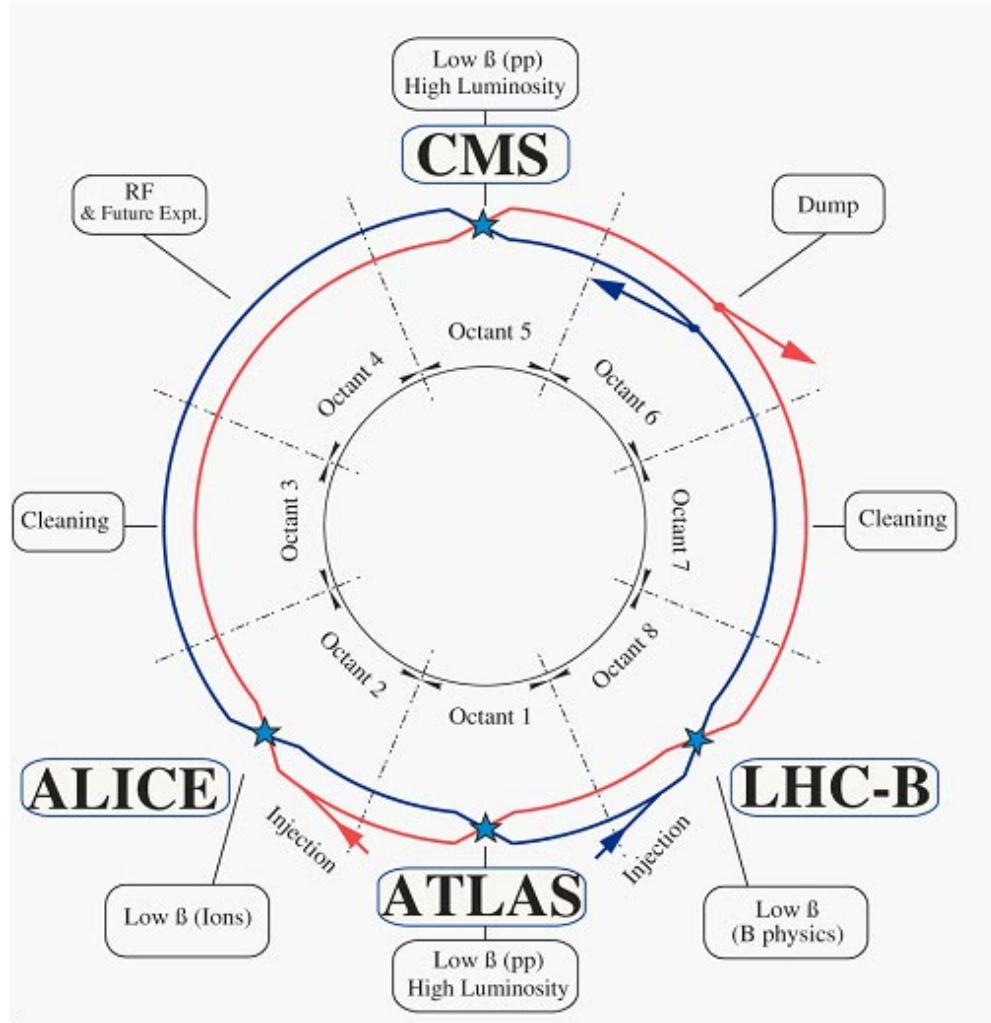


Figure 3.2: Labeled diagram of all the experiments at the LHC indicating the counter circulating beams and points of interest along the circumference of the accelerator.

375 The exact design of the tunnel is due to the experimental constraints of the original
 376 machine for which it was built, the Large Electron Positron (LEP) Collider. For the
 377 $\sim 2,000$ times lighter electron the maximum energy was limited by the synchrotron
 378 radiation, proportional to $\frac{1}{m^4}$, requiring long straight sections of accelerating RF cavities
 379 to recouperate the lost energy. Given that this effect is $\mathcal{O}(10^{13})$ times smaller for the
 380 proton the LHC is instead limited by our ability to design and construct magnets strong
 381 enough to bend the beam given the already determined curvature of the 8 arcs.

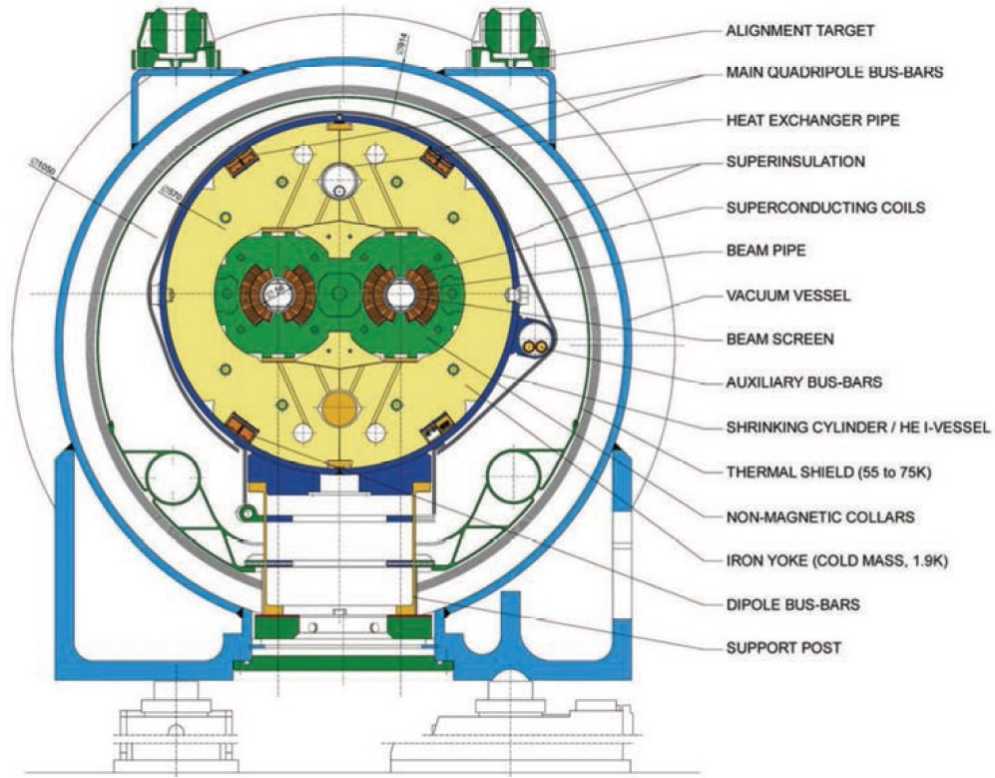


Figure 3.3: Depiction of a LHC dipole magnet 2-in-1 design labeling the major components

382 The oppositely circulating beams must each have their own ring and magnetic field
383 which lead to the creation of a twin-bore (i.e. "two-in-one") magnet design, a cross
384 section of which can be seen in figure 3.3. These magnets are constructed using NbTi
385 superconductors which are cooled to 2K using superfluid helium. These magnets are
386 designed to provide the needed 8.33 T magnetic field required to bend the beams at the
387 design beam energy of 7 TeV. In total 1231 of these 15 m long bending dipole magnets
388 are used, in association with 392 5-7m long quadrupole magnets which are responsible
389 for keeping the proton bunches in a tight beam by squeezing them either horizontally
390 or vertically.

391 **3.3 Performance**

392 Since the begining of its stable running in 2010 the LHC has performed well, even
393 exceeding our expectations. While the experiment itself is incredibly complex, the
394 performance of the machine, for the purposes of our analysis, can be reduced to two
395 numbers; the familiar center of mass energy of the beams and a less common quantity
396 known as the integrated luminosity.

397 For particle physics the integrated luminosity is proportional to the total number of
398 collisions recorded during a specified time period, while the instantaneous luminosity is
399 proportional to the bunch crossing rate along with the cross section of a proton-proton
400 interaction and represents the potential number of collisions per second. Knowing this

401 we can see that the integrated luminosity, L_{int} is simply the integral of the instantaneous
 402 luminosity $L_{inst.}$ for a choosen data period as seen in equation 3.1.

$$L_{int} = \int L_{inst.} dt \quad (3.1)$$

403 For a standard Gaussian beam, $L_{inst.}$ can be written as

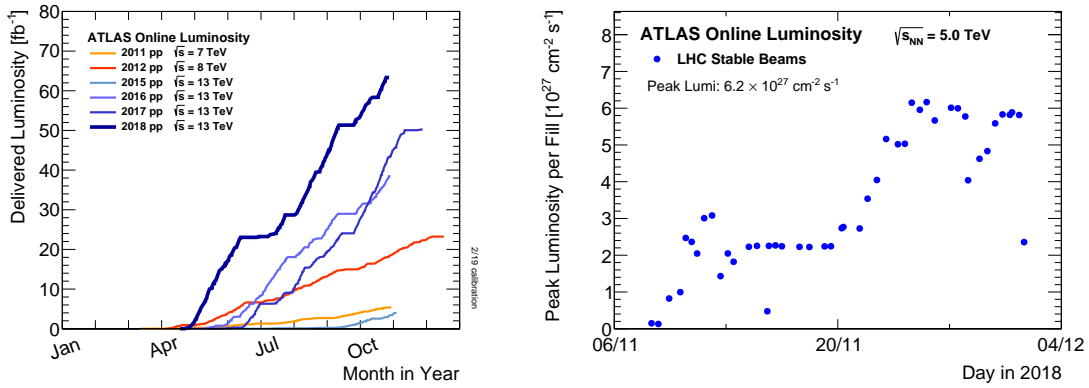
$$L = \frac{N_b^2 n_b f_{rev} \gamma_r}{4\pi \epsilon_n \beta^*} F \quad (3.2)$$

404 where N_b is the number of particles per bunch, n_b the number of bunches per beam,
 405 f_{rev} the revolution frequency, γ_r the relativistic gamma factor, ϵ_n the normalized trans-
 406 verse beam emittance, β^* the beta function at the collision point, and F the geometric
 407 luminosity reduction factor due to the crossing angle at the interaction point given by

$$F = \left(1 + \left(\frac{\theta_c \sigma_z}{2\sigma^*} \right)^2 \right)^{-1/2} \quad (3.3)$$

408 where θ_c is the full crossing angle at the interaction point, σ_z is the RMS bunch length,
 409 and σ^* is the transverse RMS beam size at the interaction point.

410 For the ATLAS experiment the integrated luminosity for each year can be seen in figure
 411 3.4a as well as an example of the instantaneous luminosity for the choosen year in figure
 412 3.4b.



(a) Integrated Luminosity 2011 - 2018 (b) 2018 Peak Instantaneous Luminosity

Figure 3.4: Luminosity is monitored as both a running total known as the Integrated Luminosity as depicted in (a) and as an instantaneous quantity as shown in (b)

3.4 Pile-up at the LHC

Given the large number of protons per bunch and the cross-section of a proton-proton interaction, the probability to observe multiple interactions per bunch crossing is quite high. These multiple-interaction are known as pile-up, μ or the time averaged representation $\langle\mu\rangle$, and come in two different forms:

1. **In-time pile-up:** These are the other proton-proton collisions that occur during the same bunch crossing as the primary interaction that caused the Data Acquisition (DAQ) system to trigger. These are the standard extra interactions we expect to observe as stated above.
2. **Out-of-time pile-up:** These are interactions that occur either before or after a

423 bunch crossing that causes the DAQ to trigger. This effect is generally due to the
 424 long integration times of some detector electronics.

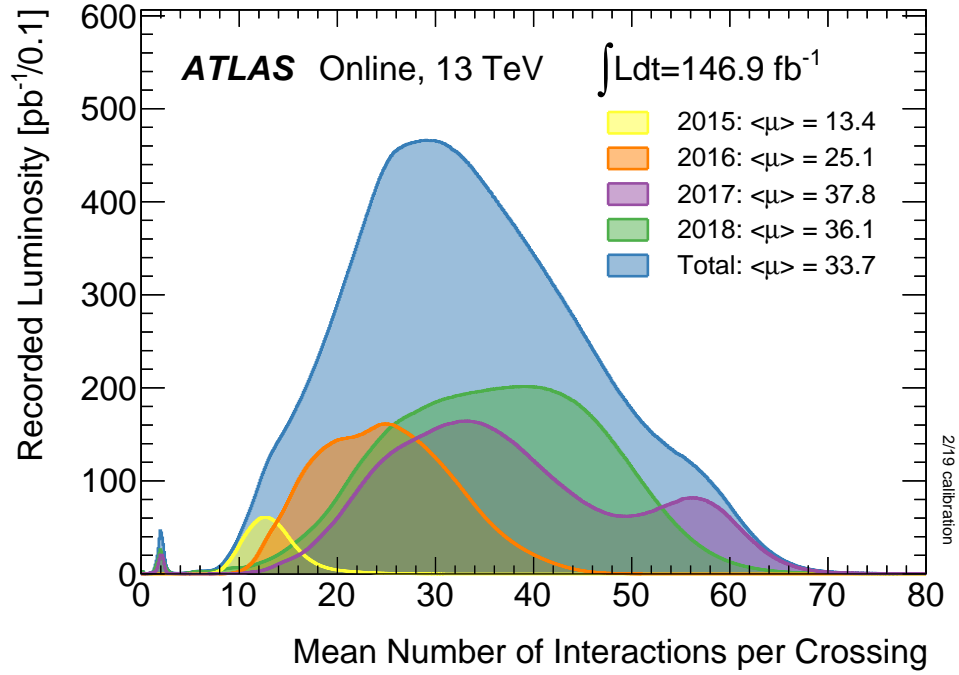


Figure 3.5: Pileup for data taking periods 2015 - 2018

425 The pile-up profile for past years can be seen in figure 3.5. The width of this distributino
 426 is due a combination of Poissonian statistics, the decrease in number of protons per bunch
 427 over the lifetime of a single run, and optimization tweaks to the beam's profile during
 428 runtime. Understanding and eliminating the noise from these pile-up events is crucial
 429 to reconstructing physics variables to represent the primary interaction we hope to
 430 observe.

431 Chapter 4

432 The ATLAS Detector

433 Given the immense energies available at the LHC, and the veritable zoo of particles we
434 are trying to detect, we require a general-purpose experiment in order to fully exploit
435 the full range of physics opportunities provided. Two international collaborations rose
436 to this challenge, the CMS (Compact Muon Solenoid) and ATLAS (A Torroidal LHC
437 ApparatuS) experiments. While both have similar physics goals and each of them
438 strengths and weaknesses, this dissertation will focus on the ATLAS experiment and
439 the intricacies of its three main sub-detectors and two massive magnet systems depicted
440 in figure 4.1.

441 Originally proposed in 1994 the ATLAS experiment was completed in 2008. On July
442 4th, 2012 in a joint announcement the ATLAS and CMS experiments announced the
443 discovery of the long predicted Higgs Boson. The collaboration now boasts over 3000
444 physicists from 175 institutions spread across 38 countries and continues to probe

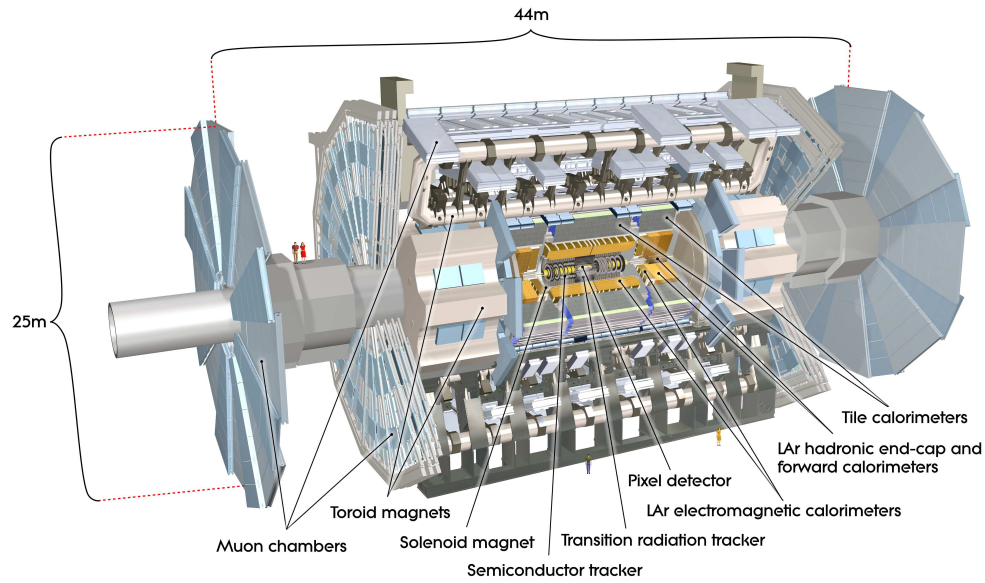


Figure 4.1: [3] Here we see a cut-away side view of the ATLAS detector with the major components labeled. Note that within each of these labeled components there may exist multiple different detector technologies. For scale two people in red are shown standing between the disk muon chambers on the left side of the figure.

445 the limits of the Standard Model in pursuit of answers to some of Humanities deepest
446 questions.

447 Located approximately 100 meters underground in a vast excavated chamber, the AT-
448 LAS detector rests its 7000 metric tonnes on a bed of concrete reinforced steel. Out of
449 it flows the signals of over 100 million electronic channels through a zip tied mass of
450 greater than 3000 kilometers of cabling. At its very center is one of the four interaction
451 points of the LHC, specifically Point 1, where the two counter circulating proton beams
452 are skillfully shaped and then collided by a series of magnets. The energetic particles
453 resultant from this collision then fly out in all directions into the bulk of the ATLAS
454 detector.

455 The first sub-system they meet is the Inner Detector (ID) and its many layers of strip
456 and pixel silicon detectors along with a transition radiation gaseous wire detector, all
457 bathed in the 2T magnetic field of the surrounding superconducting solenoidal magnet.
458 This system exploits the ionization of charged particles to track their curved trajectory
459 through the magnetic field. This curvature gives us charge information, a momentum
460 measurement, and precision 3D vertices crucial to the identification of the secondary
461 vertices of a b-hadron decay.

462 Outside of the solenoid the particles are faced with first the Electromagnetic and then
463 the Hadronic sampling calorimeters. Here, layers of scintillator and high radiation length
464 materials are implemented to measure the energy of electrons, photons, and hadrons.
465 As the goal is to completely absorb the energy of all outgoing particles the calorimeter

466 has a nearly 4π solid angle coverage.

467 Finally we have the muon system surrounding the calorimeter and equipped with its
468 own torroidal magnet system. Here the charged muon bends in the magnetic field
469 while leaving a trail of ionization in the muon spectrometer before exiting the detector
470 completely. Neutrinos are the only other standard model particle that leave the detector,
471 however they do so without detection. A depiction of the various particle interactions
472 with the different detector sub-systems can be seen in figure 4.2

473 In the following sections I will explain our choosen coordinate system and give a more
474 detailed reveiw of these 3 detector sub-systems.

475 4.1 ATLAS Coordinate System

476 Using the nominal interaction point as the origin, ATLAS uses a right handed coor-
477 dinate system where the positive x -axis points towards the center of the LHC ring,
478 the positive y -axis points upwards, and the positive z -axis is defined by the counter
479 clockwise circulating beam direction as viewed from above shown in figure 4.3 [3].

480 Using these coordinates we can define the physical momentum of the objects measured
481 as $\vec{p} = (p_T, p_z)$ with p_T being the momentum of the object in the transverse plane and
482 p_z the momentum along the beam axis. Given the cylindrical symmetry of ATLAS it
483 is desireable to define the polar angle θ from the beam axis with the $r - \phi$ plane being
484 perpendicular to that axis. Since the particles we observe are relativistically boosted

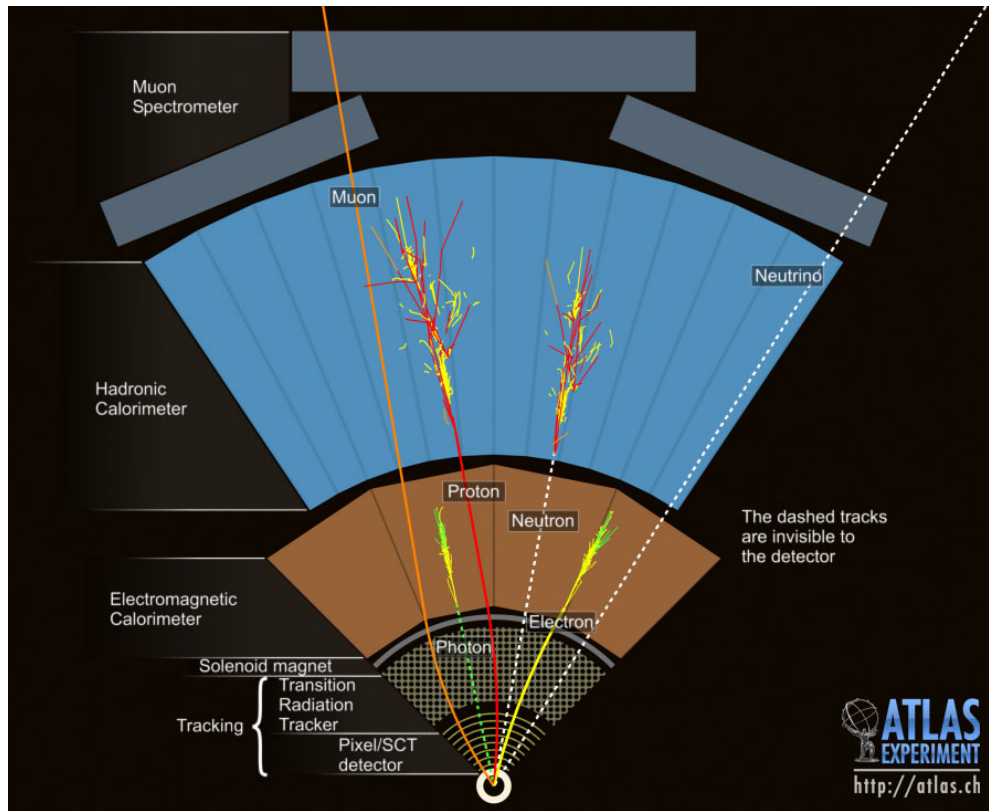


Figure 4.2: This slice of the ATLAS detector depicts how different particles interact with each component of the detector it crosses. A dashed line indicates no interaction while a solid line indicates interaction. Electrons (yellow/green) and charged hadrons (red) interact with the tracker and curve in the solenoid's magnetic field. Electrons and photons (yellow/green) are absorbed by the Electromagnetic calorimeter. All hadrons (red/yellow) are absorbed by the Hadronic calorimeter. The muons (orange) curve in both the solenoid and torroid magnetic fields before exiting the detector. Finally, the neutrinos (white) pass through the entire detector without interacting.

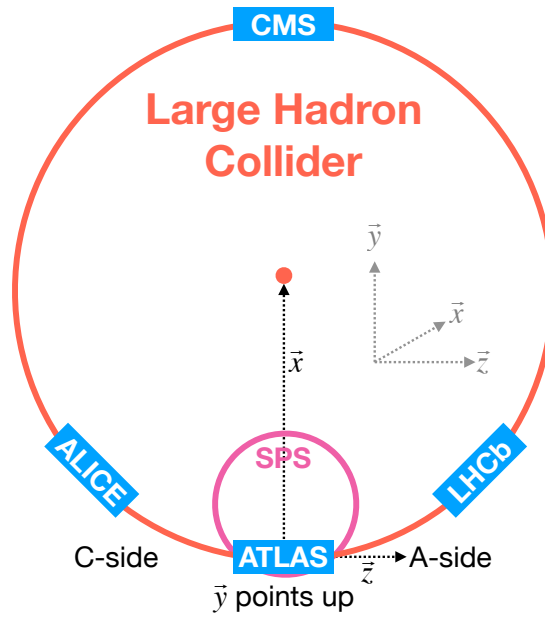


Figure 4.3: [4] A cartoon view of the the LHC from above showing the SPS, LHC and the four main experiments of the LHC: ATLAS, CMS, LHCb, and ALICE. The standard cartesian coordinate system is shown with its origin at the ATLAS interaction point, the positive x -axis towards the center of the LHC, the positive y -axis pointing upwards, and the positive z -axis pointing along the beamline towards the "A-side"

485 in the z -axis it is desirable to use the Lorentz invariant quantity pseudorapidity (η)
 486 defined in terms of the polar angle by

$$\eta = -\ln \tan \left(\frac{\theta}{2} \right). \quad (4.1)$$

487 where $\eta = 0$ is in the $x - y$ plane and larger values of $|\eta|$ being closer to the beam axis
 488 as can be seen in figure 4.4.

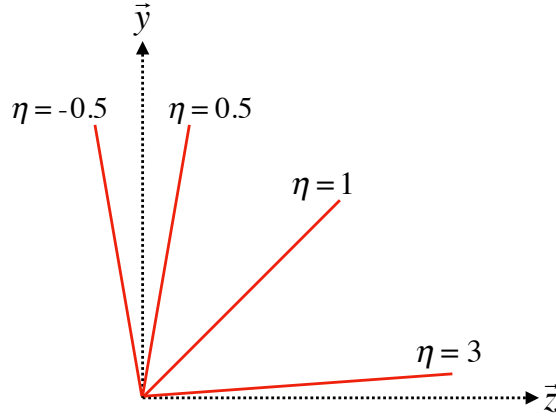


Figure 4.4: Modified from [4] this cartoon represents a selection of pseudorapidity (η) values overlaid with some cartesian coordinates (dashed black lines). The redlines are drawn for $\eta = \pm 0.5, 1.0, 3.0$

489 In this analysis the angular separation between objects in the detector is calculated and
 490 represented using the geometric quantity

$$\Delta R = \sqrt{(\Delta\eta)^2 + (\Delta\phi)^2} \quad (4.2)$$

4.2 Tracking with the Inner Detector

With its closest component, the insertable b-layer (IBL) [5], only 3.3 cm from the interaction point The Inner Detector (ID), shown in figure 4.5 [6, 7], faces the incredible challenge of providing precision momentum resolution and identification of both primary and secondary vertex measurements of charged tracks all while receiving the highest fluence.

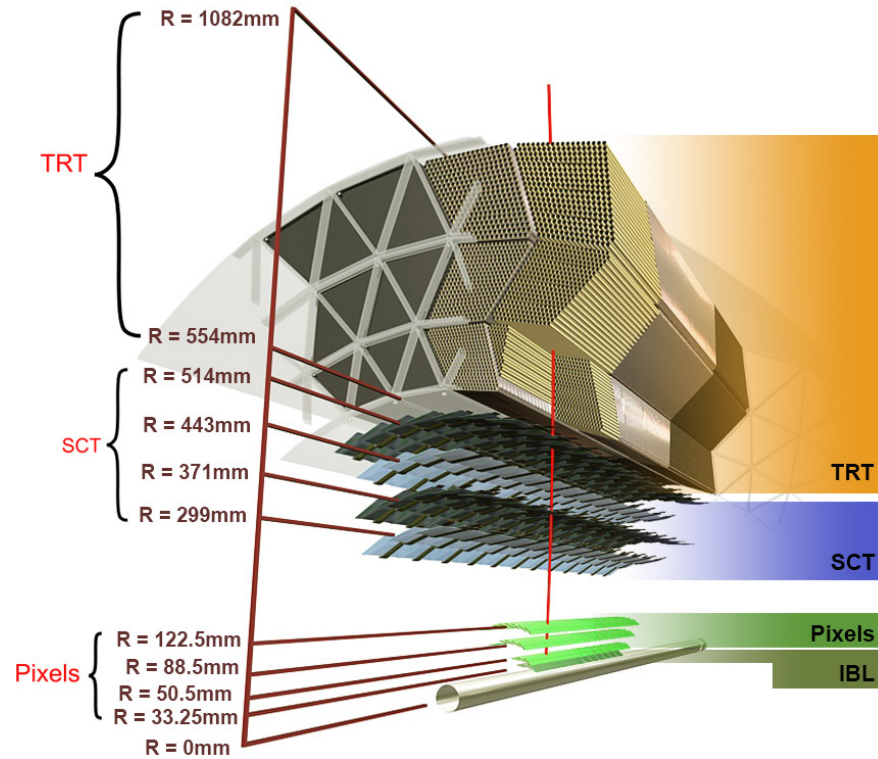


Figure 4.5: [5] Diagram of inner detector

It is designed to be very compact to reduce the probability of a particle decaying inside and to give precision measurements of the particles curvature in the 2T solenoidal

499 magnetic field. This leads to excellent momentum resolution above the nominal p_T
500 threshold of 0.5GeV and within the pseudorapidity range of $|\eta| < 2.5$ as shown in figure

501 4.6

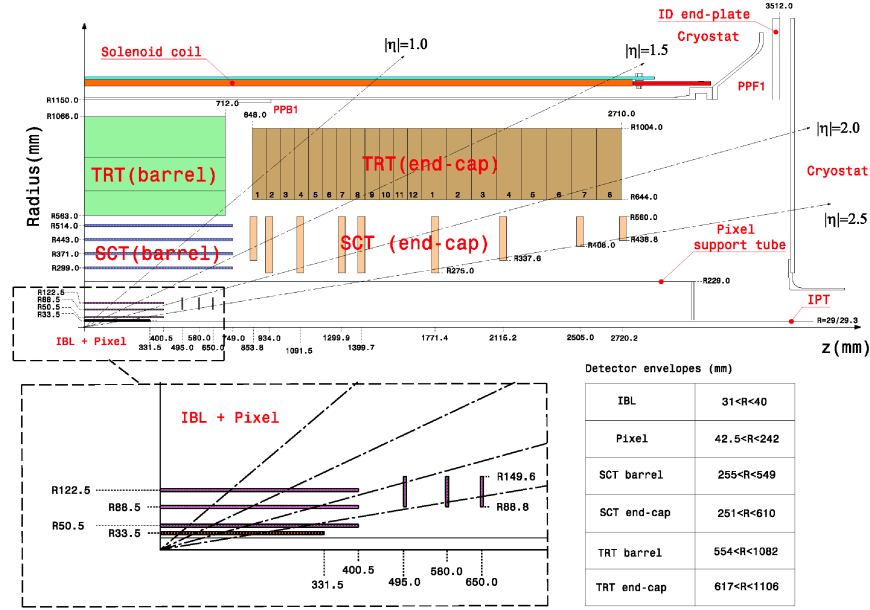


Figure 4.6: [8] Schematic of the Inner Detector including eta lines. Each component shown is cylindrically symmetric leading to a multi-layered detector.

502 The ID is composed of three different detector technologies for particle trajector re-
503 construction: The Pixel Detector, Semiconductor Tracker (SCT) and the Transition
504 Radiation Tracker (TRT). These will be discussed in the following sections.

505 4.2.1 Pixel Detector

506 The ATLAS Pixel Detector [3], the innermost subdetector of the ID, is designed to
507 give the best resolution possible as close as possible to the interaction point. This
508 is accomplished using the 4 barrel layers and the 3 disks per endcap as indicated in
509 figure 4.6. The inner most barrel layer, the IBL, has pixel dimensions of $50\mu\text{m}(\hat{\phi}) \times$
510 $250\mu\text{m}(\hat{z}) \times 200\mu\text{m}(\hat{r})$. For the other layers the dimensions are $50\mu\text{m}(\hat{\phi}) \times 400\mu\text{m}(\hat{z})$ for
511 about 90% of the pixels and $50\mu\text{m}(\hat{\phi}) \times 600\mu\text{m}(\hat{z})$ for the others, all with a thickness
512 of $250\mu\text{m}(\hat{r})$. This gives a total active area of 1.88m^2 collected through 92.4 million
513 readout channels, more than half of the total number of channels for ATLAS. This
514 detailed charged particle information very close to the interaction point is crucial not
515 only for pattern recognition for track reconstruction, but also for the reconstruction
516 of the primary and secondary vertices intrinsic to the decay of a b -hadrons, a critical
517 element of the analysis presented in this thesis.

518 4.2.2 Semiconductor Tracker

519 Encompassing the Pixel Detector, the Semiconductor Tracker (SCT) [3] is composed of
520 double sided silicon microstrips modules. Each side of the 4088 modules is constructed
521 out of two silicon strip sensors that are daisy chained together. The result is 768
522 composite strips each 12.6cm with an inter-strip pitch of $80\mu\text{m}$. In the barrel the strips
523 are aligned with the \hat{z} direction, while in the end caps they are aligned with the \hat{r}
524 direction. In both cases the separation of the strips is constant in $\hat{\phi}$. The two sides are

525 rotated with respect to each other by $40\mu\text{m}$ to allow for position measurement along the
526 length of the strip. These modules are then used to tile the 4 barrel layers and 9 disks
527 per endcap (18 disks in total) as seen in figure 4.6. This design is chosen to ensure
528 that each charged track interacts with 8 strip layers (equivalent to four space points).
529 This information is used to further measure the momentum and impact parameter, and
530 as well as vertex identification of charged particles.

531 4.2.3 Transition Radiation Tracker

532 The Transition Radiation Tracker [3], the outermost subdetector of the ID, provides
533 tracking through the detection of transition radiation from ultra-relativistic charged
534 particles for $\eta < 2.0$ using 350,000 drift tube channels also known as straws. The
535 4mm diameter straws are filled with a 70% Xe, 27% CO₂, and 3% O₂ gas mixture
536 and a $31\mu\text{m}$ diameter gold-plated tungsten wire anode at the center for the collection
537 of the ionization signal. In the barrel 73 azimuthally symmetric layers of 144cm straws
538 are oriented parallel to the beam pipe with an electrical division in the center of each
539 allowing the two sides to be read out separately. For each endcap the straws are radially
540 oriented in 160 symmetric planes each containing 768 37cm long drift tubes shown
541 in figure 4.6. In both the barrel and the end caps polypropylene fibers (barrel) or
542 foils (encaps) function as the transition radiation material which causes the relativistic
543 charged particles to radiate and thus ionize the gas in the straw. The amount of
544 transition radiation produced is proportional to the Lorentz factor meaning that lighter

particles (e.g. electrons) will produce more radiation. Thus, by defining a high and low threshold, we can identify tracks belonging to electrons by requiring they register more high-threshold hits. There are typically 36 TRT hits per charged track.

4.3 Calorimetry

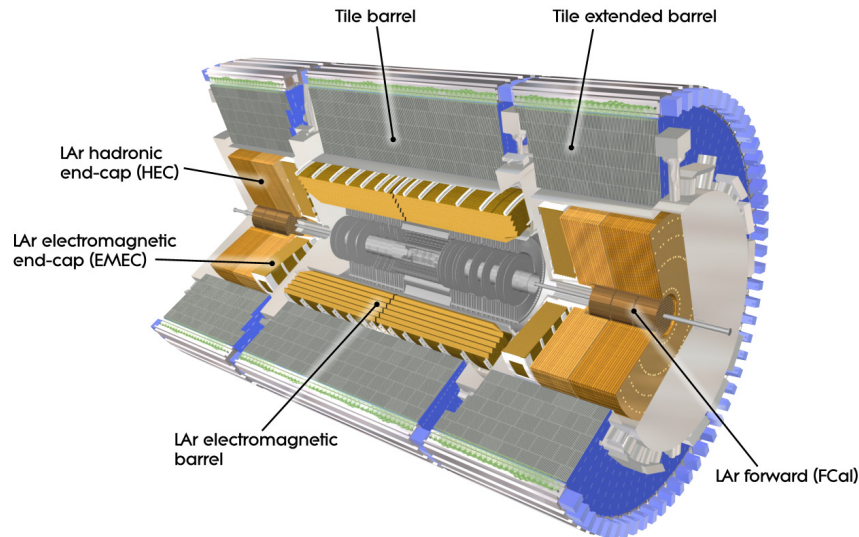


Figure 4.7: [3] A cutaway diagram of ATLAS's sampling calorimeters

Once the proton collision remnants have passed through the ID and its surrounding solenoid they enter into the ATLAS calorimeters depicted in figure 4.7. Sampling calorimeter technologies were chosen for their compact geometry and lower cost point. These are constructed by alternating layers of absorber, a dense material which reduces the incident particles energy, and active material which produces a detectible signal when a particle passes through. This means that the detected signal is only a fraction

555 of the total energy of the particle and thus requires a study of the calorimeter response
 556 for calibration purposes [9]. The first system, the Electromagnetic Calorimeter (EMC),
 557 is designed to measure the energy of electrons and photons which primarily lose their
 558 energy via bremsstrahlung and pair production electromagnetic interactions. Outside of
 559 the EMC is the Hadronic Calorimeter (HC) which is designed to measure the energy of
 560 jets of hadrons through their electromagnetic and strong interactions. These detectors
 561 cover the entire $|\eta| < 4.9$ range and provide complete containment of both Electromag-
 562 netic and Hadronic showers with higher granularity in the EMC for $|\eta| < 2.5$, the region
 563 matched to the ID, for precision measurements of electrons and photons. By instrument-
 564 ing this huge space in $|\eta|$ we can search for events with asymmetric energy deposits which
 565 imply the existence of a particle we didn't detect represented by missing transverse
 566 energy E_T^{miss} .

567 **4.3.1 Electromagnetic Calorimeter**

568 The innermost calorimeter, the Liquid Argon (LAr) Electromagnetic Calorimeter (EMC)
 569 [3], uses lead as the absorber and liquid argon as the active material in an "accordion
 570 geometry" as seen in figure 4.8. This geometry was chosen for uniform coverage in
 571 $\hat{\phi}$ due to its lack of un-instrumented cracks in the radial direction. The barrel region
 572 covers $|\eta| < 1.475$ and an end cap on each side covers $1.375 < |\eta| < 3.2$ each housed
 573 in their own cryostat. The barrel is composed of two half barrels with a 4mm gap at
 574 $z = 0$ and both end caps are divided into an inter wheel covering $2.5 < |\eta| < 3.2$ and

575 an outer wheel covering $1.375 < |\eta| < 2.5$.

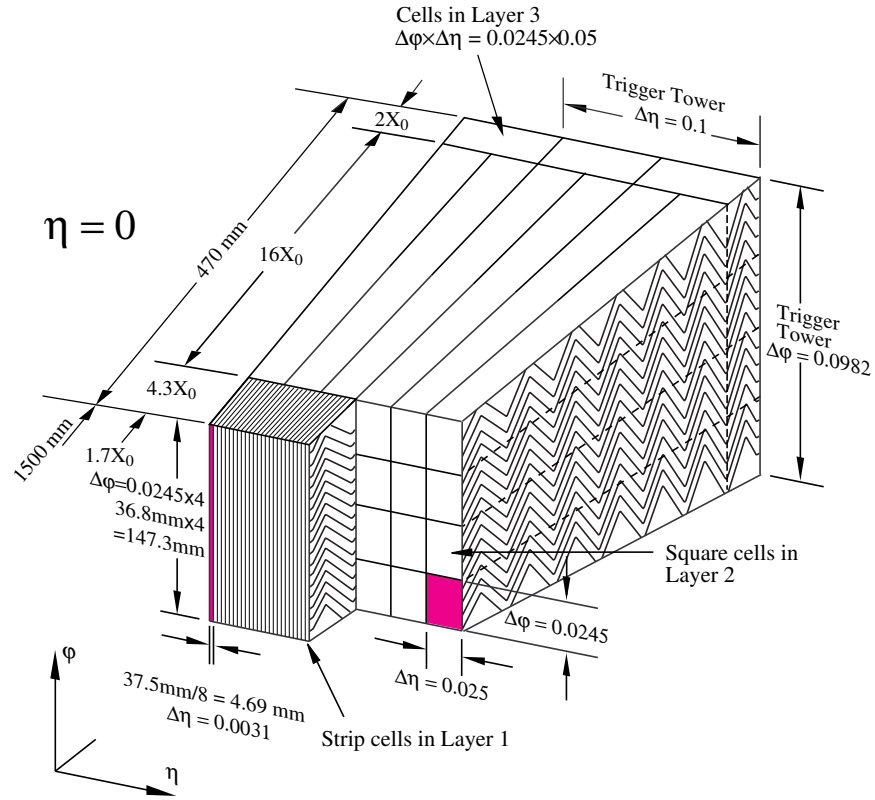


Figure 4.8: [3] Sketch of LAr EMC barrel module where the lead and liquid argon layers are visible in an accordion like geometry. Looking from the foreground to the back there are 3 different types of cells visible.

576 In the $|\eta| < 2.5$ region the EMC has 3 radial layers for precision physics measure-
 577 ments. Layer 1 consists of strip cells which are finely segmented with $\Delta\eta = 0.0031$
 578 and $\Delta\phi = 0.0245$ allowing for precision position resolution which gives discrimination
 579 power between a single γ deposit and the π^0 characteristic $\gamma\gamma$ deposit. Layer 2 , which
 580 collects the largest fraction of energy from electromagnetic shower, is segmented with

581 $\Delta\eta = .025$ and $\Delta\phi = 0.0245$. Layer 3 collects the tail of the electromagnetic shower
 582 using a coarser segmentation of $\Delta\eta = .05$ and $\Delta\phi = 0.0245$. Additionally, in the region
 583 $|\eta| < 1.8$ a thin pre-sampler, which contains no lead absorber, was placed in front of
 584 Layer 1 to allow for energy corrections due to losses upstream of the EMC. Combined
 585 the EMC is > 22 radiation lengths (X_0) in the barrel and $> 24 X_0$ in the end-caps,
 586 where a radiation length is the average distance an electron travels in a given material
 587 before losing $1/e$ of its original energy E_0 via bremsstrahlung radiation.

588 4.3.2 Hadronic Calorimeter

589 Directly outside the EMC envelope is the Hadronic Calorimeter (HC) system [3] which
 590 consists of three sampling calorimeter technologies: the Tile calorimeter, the LAr
 591 hadronic end-cap calorimeter (HEC) and the LAr forward calorimeter (FCal). Com-
 592 bined, these three subsystems give measurements of hadronic jet energies in the $0 <$
 593 $|\eta| < 4.9$ range. The tile calorimeter uses steel as the absorber layer and scintillating
 594 tiles as the active material and covers the region $|\eta| < 1.7$ with a barrel section flanked
 595 by two barrel extensions each divided azimuthally into 64 modules. These scintillator
 596 tiles are read out on two sides by wave-length shifting fibers connected to photomul-
 597 tiplier tubes as seen in figure 4.9. At $\eta = 0$ the total tile calorimeter thickness is 9.7
 598 nuclear interaction lengths (λ), where λ is the average distance a hadron travels before
 599 interacting inelastically with a nucleus.

600 The HEC is composed of two independent wheels per end-cap located just past the

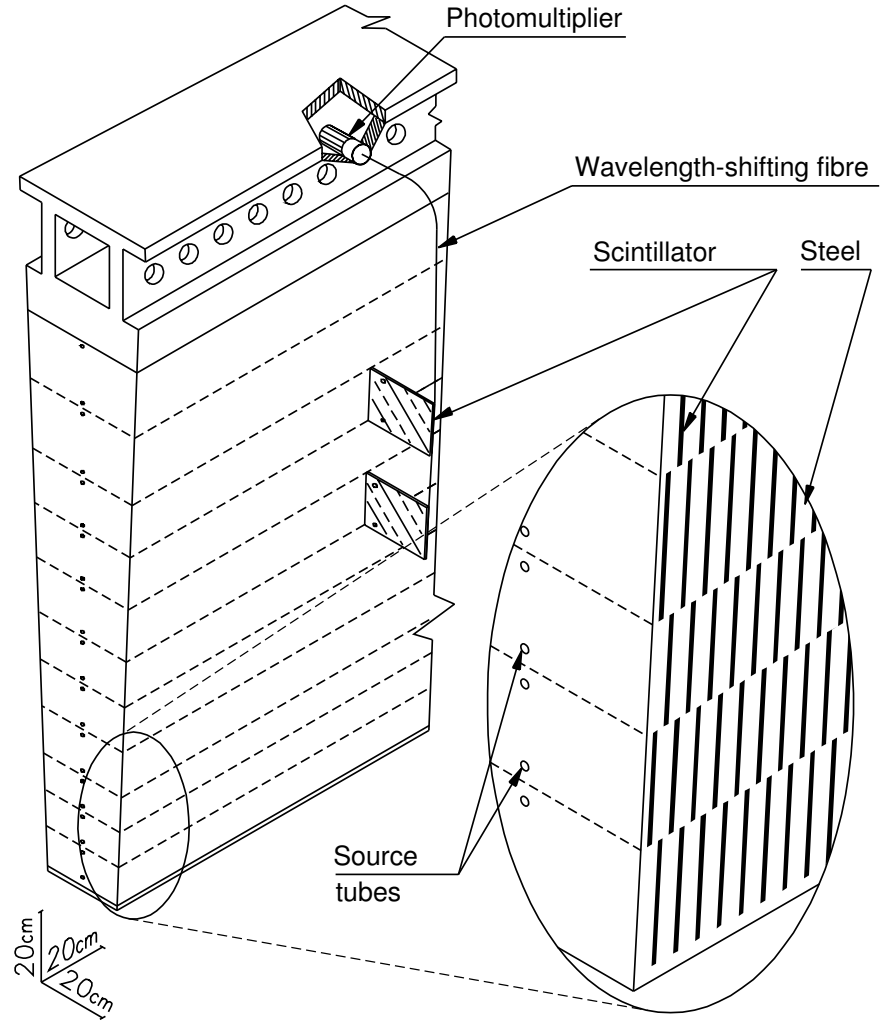


Figure 4.9: [3] Schematic of a tile calorimeter module including a depiction of the connection between the scintillator tile to the photomultiplier via a wavelength-shifting fibre.

601 EMC end-cap but sharing the same cryostat. This system uses copper as an absorber
 602 and liquid argon for the active material and covers the $1.5 < |\eta| < 3.2$ range using
 603 32 wdg-shaped modules per wheel. Finally, the FCal shares the same cryostat as the
 604 EMC and HEC end-caps and acts to extend the coverage of the combined calorimeter
 605 system to include the $3.1 < |\eta| < 4.9$ range. Each endcap contains 3 modules, the first
 606 an electromagnetic module (Copper/Liquid-Argon) which is followed by two hadronic
 607 modules which use (Tungsten/Liquid-Argon).

608 **4.4 Muon Spectrometer**

609 The ATLAS Muon Spectrometer (MS) [3], see figure 4.10, accomplishes tracking of
 610 charged particles in the $|\eta| < 2.7$ region for momentum reconstruction while also provid-
 611 ing triggering on charged particles in the $|\eta| < 2.4$ region. The magnetic field necessary
 612 for momentum reconstruction is provided by 3 air core torroid systems, one barrel tor-
 613 roid covering $|\eta| < 1.4$ and two endcap torroid systems which are inserted into the inner
 614 radius of the the barrel torroid to cover the $1.6 < |\eta| < 2.7$. The so called transition
 615 region $1.4 < |\eta| < 1.6$ between these two magnet systems is covered by a combination
 616 of the barrel and endcap torroid magnets. Similar to the ID the resolution is inversely
 617 proportional to the particle's incident momentum. Any muon with pT lower than 3GeV
 618 will never make it to the MS and thus will not be detected.

619 Precision tracking measurements for momentum reconstruction is accomplished using

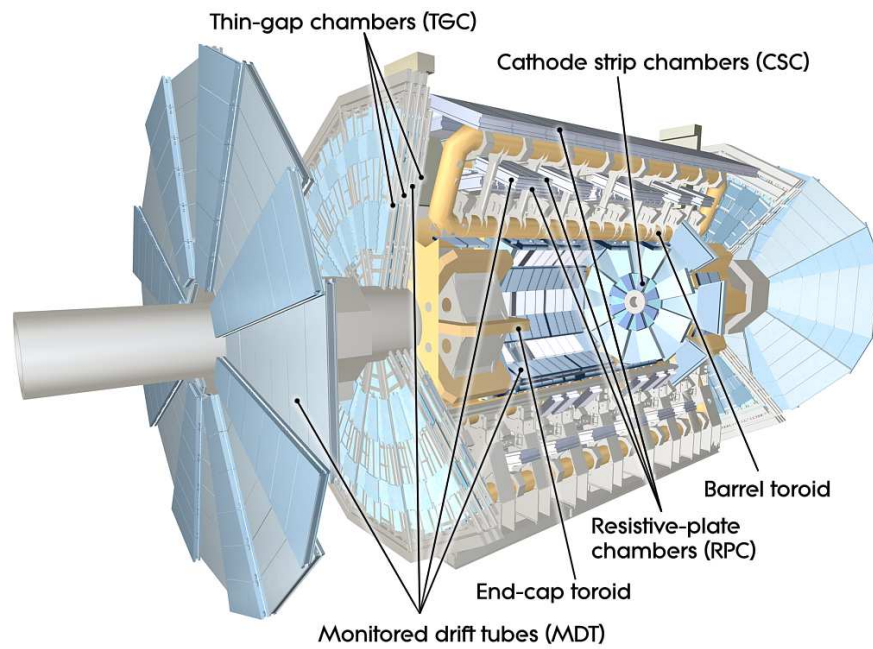


Figure 4.10: [3] A cut-away diagram of the ATLAS muon system and its many sub-detectors.

620 the Monitored Drift Tube chambers (MDTs) for $|\eta| < 2.0$ and using Cathode-Strip
621 Chambers (CSCs) for $2.0 < |\eta| < 2.7$. The MDT system consists of 1163 drift tube
622 chambers arranged in three to eight layers for varying η . The CSCs are designed to
623 withstand the higher rate and retain good time resolution using multiwire proportional
624 chambers with orthogonal segmented cathode planes.

625 The MS also gives nanosecond tracking information for triggering on muon tracks. This
626 is accomplished using Resistive Plate Chambers (RPC) in the barrel region $|\eta| < 1.05$
627 and Thin Gap Chambers (TGC) in the end-cap $1.05 < |\eta| < 2.4$ region. Both chamber
628 systems deliver a triggerable signal with a spread of 15–25 ns, thus providing the ability
629 to tag individual beam-crossings.

630 Chapter 5

631 Boosted Higgs at the LHC

632 Its July 4th, 2012 and the walls of building 500 are reverberating as Particle Physicists
633 around the world rejoice the discovery of the particle that gives all things mass, the
634 Higgs Boson.

635 **5.1 Physics beyond the Standard Model**

636 **5.2 Higgs Production Mechanisms**

637 **5.3 Branching Ratios**

638 **5.4 Discovery**

639 **5.5 Fermion Decay Modes**

640 **5.6 Boosted Higgs**

641

Part III

642

The HbbISR Analysis

643 Chapter 6

644 Data and Simulation Preparation

645 In order to compare data to theory ATLAS has developed an analysis chain which runs
646 both real data and simulated samples through the same processing, assuring a final
647 result which is as comparable as possible.

648 6.1 Data Used

649 6.2 Monte Carlo Samples

650 Chapter 7

651 Physics Object Selection

652 After the ATHENA Digitization step both data and monte carlo have the same format,
653 representing the three dimentional energy deposits. In order to analyze these deposits
654 they are cleaned, clustered and checked for overlap resulting in physics objects useful
655 for our specific analysis.

656 **7.1 Calorimeter Jets**

657 **7.2 Track Jets**

658 **7.3 Fat Jets**

659 **7.4 B-tagged Jets**

660 **7.5 Muons**

661 **7.6 Overlap Removal**

662 Chapter 8

663 Event Selection

664 Having created our physics objects we begin to make selections of what types of events
665 we want to consider given the goal of our analysis. In our boosted topology this means
666 considering things like momentum, jet collection efficiencies and background rejection.

667 8.1 Selected Triggers

668 8.2 Pre-selection Studies

669 8.3 Signal Selection

670 8.4 Optimisation

671 Chapter 9

672 Background Estimation

673 The dominant background was QCD. I worked on the $t\bar{t}$ control region. The V_{qq}
674 and single top backgrounds were estimated from monte carlo.

675 9.1 Multi-jet QCD estimation

676 9.2 $t\bar{t}$ control region

677 9.3 Single top estimation

678 9.4 Hadronic vector boson channel

679 Chapter 10

680 Systematic Uncertainties

681 10.1 Theoretical Uncertainties

682 10.2 Experimental Uncertainties

683 **Chapter 11**

684 **Statistical Fit**

685 The statistical fit in our analysis was accomplished using a framework developed for
686 Higgs searches.

687 **11.1 Profile Likelihood Function**

688 **11.2 Fit Configuration**

689 **11.3 Statistical Tests**

690 **Chapter 12**

691 **Results**

692 **12.1 Expectations**

693 **12.2 Statistical Analysis Results**

694 **12.3 Measurements and Limits**

695

Part IV

696

Conclusion

697 Chapter 13

698 Conclusion

699 I conclude that this section is the conclusion

Bibliography

- [1] Lyndon Evans and Philip Bryant. “LHC Machine”. In: *JINST* 3 (2008), S08001. DOI: 10.1088/1748-0221/3/08/S08001 (cit. on p. 16).
- [2] Chris Llewellyn Smith. “Genesis of the Large Hadron Collider”. In: *Phil. Trans. Roy. Soc. Lond.* A373.2032 (2014), p. 20140037. DOI: 10.1098/rsta.2014.0037 (cit. on p. 16).
- [3] ATLAS Collaboration. “The ATLAS Experiment at the CERN Large Hadron Collider”. In: *JINST* 3 (2008), S08003. DOI: 10.1088/1748-0221/3/08/S08003 (cit. on pp. 27, 29, 35–43).
- [4] Giordon Holtsberg Stark. “The search for supersymmetry in hadronic final states using boosted object reconstruction”. Presented 26 Apr 2018. May 2018. URL: <https://cds.cern.ch/record/2317296> (cit. on pp. 31, 32).
- [5] Karolos Potamianos. *The upgraded Pixel detector and the commissioning of the Inner Detector tracking of the ATLAS experiment for Run-2 at the Large Hadron Collider*. Tech. rep. ATL-PHYS-PROC-2016-104. 15 pages, EPS-HEP 2015 Proceed-

- 715 ings. Geneva: CERN, Aug. 2016. URL: <https://cds.cern.ch/record/2209070>
716 (cit. on p. 33).
- 717 [6] *ATLAS inner detector: Technical Design Report, 1*. Technical Design Report AT-
718 LAS. Geneva: CERN, 1997. URL: <http://cds.cern.ch/record/331063> (cit. on
719 p. 33).
- 720 [7] S Haywood et al. *ATLAS inner detector: Technical Design Report, 2*. Technical
721 Design Report ATLAS. Geneva: CERN, 1997. URL: [https://cds.cern.ch/](https://cds.cern.ch/record/331064)
722 [record/331064](https://cds.cern.ch/record/331064) (cit. on p. 33).
- 723 [8] B. Abbott et al. “Production and integration of the ATLAS Insertable B-Layer”.
724 In: *JINST* 13 (2018), T05008. DOI: 10.1088/1748-0221/13/05/T05008. arXiv:
725 1803.00844 [physics.ins-det] (cit. on p. 34).
- 726 [9] Christian Wolfgang Fabjan and F Gianotti. “Calorimetry for Particle Physics”.
727 In: *Rev. Mod. Phys.* 75.CERN-EP-2003-075 (Oct. 2003), 1243–1286. 96 p. DOI:
728 10.1103/RevModPhys.75.1243. URL: <https://cds.cern.ch/record/692252>
729 (cit. on p. 38).

⁷³⁰ **Appendix A**

⁷³¹ **Hadronic Vqq Sherpa Studies**

⁷³² Ancillary material should be put in appendices, which appear after the bibliography.